PNAS RESEARCH ARTICLE | EARTH, ATMOSPHERIC, AND PLANETARY SCIENCES

Upstream surface roughness and terrain are strong drivers of contrast in tornado potential between North and South America

Funing Li[a,1,2], Daniel R. Chavas[a], Brian Medeiros[b], Kevin A. Reed[c], and Kristen L. Rasmussen[d]

Edited by Richard Rotunno, National Center for Atmospheric Research, Boulder, CO; received September 6, 2023; accepted April 30, 2024

Central North America is the global hotspot for tornadoes, fueled by elevated terrain of the Rockies to the west and a source of warm, moist air from equatorward oceans. This conventional wisdom argues that central South America, with the Andes to the west and Amazon basin to the north, should have a "tornado alley" at least as active as central North America. Central South America has frequent severe thunderstorms yet relatively few tornadoes. Here, we show that conventional wisdom is missing an important ingredient specific to tornadoes: a smooth, flat ocean-like upstream surface. Using global climate model experiments, we show that central South American tornado potential substantially increases if its equatorward land surface is smoothed and flattened to be ocean-like. Similarly, we show that central North American tornado potential substantially decreases if its equatorward ocean surface is roughened to values comparable to forested land. A rough upstream surface suppresses the formation of tornadic environments principally by weakening the poleward low-level winds, characterized by a weakened low-level jet east of the mountain range. Results are shown to be robust for any midlatitude landmass using idealized experiments with a simplified continent and mountain range. Our findings indicate that large-scale upstream surface roughness is likely a first-order driver of the strong contrast in tornado potential between North and South America.

tornado alley | tornado | severe thunderstorm | terrain | surface roughness

Significance

Why does the United States have the most tornadoes in the world? This work examines how a smooth, flat ocean-like upstream surface may substantially increase the potential for tornadoes downstream. This explains why North and South America both possess severe thunderstorm hotspots due to their similar geographic setup—a mountain range to the west and an equatorward source of warm, moist air—yet only North America is a hotspot for tornadoes because the equatorward ocean surface is smooth and flat. Understanding why tornado hotspots form is a foundation for understanding how they may change in a warming climate.

Tornadoes are one of the most devastating natural hazards on Earth, causing significant property losses and casualties in a few localized regions (1–7). Tornadoes tend to form from severe thunderstorms (8). In general, severe thunderstorms occur within environments characterized by i) high conditional instability, which provides a source of buoyancy to support strong updrafts; and ii) strong lower-tropospheric vertical wind shear, which supports long-lived and well-organized convection (9–18). Tornadoes typically require a third ingredient: the potential for near-ground rotation defined by intense storm-relative helicity within the lowest 1 km above the surface (SRH01), which represents horizontal vorticity that can be stretched as air flows into the storm to generate tornado rotation (19–26).

These tornadic environments are most prevalent over central North America (CNA; denoted by the box in Fig. 1*A*), particularly the Great Plains (a.k.a. Tornado Alley) (10, 27), where over 1,200 tornadoes and over 10 extreme tornado outbreaks occur annually (28, 29), an order of magnitude greater than in any other region (30–41). This behavior is commonly ascribed to elevated terrain to the west (Rocky Mountains and Mexico's Sierra Madre mountains) and equatorward oceans to the south (Gulf of Mexico and Caribbean Sea) (42–44). The north–south oriented mountain range drives the strong climatological southerly low-level flow over the Great Plains (45–47). The easterly trade winds turn northward over the east slope of the mountains and increase in speed as the flow develops anticyclonic shear vorticity (45, 46), although seasonally varying heating of the sloping terrain may also be important (47). Embedded within these southerly winds is a particularly strong flow feature known as a low-level jet (LLJ), which in this region is commonly referred to as the Great Plains low-level jet [GPLLJ; (48, 49)]. The GPLLJ is discernible throughout the day, though it is nocturnally enhanced (48, 49). This daily cycle is associated with diurnal oscillations of near-surface processes including boundary layer frictional stress (50), heating of the sloping terrain (51), and their combination (52–54). In addition, southerly winds associated with the warm sector of synoptically driven troughs are also found to enhance the southerly mean flow and LLJ over the Great Plains (42, 44, 55). This low-level southerly flow transports warm, moist near-surface air from upstream oceans into CNA (56–59) beneath a well-mixed westerly

Author affiliations: [a]Department of Earth, Atmospheric, and Planetary Sciences, Purdue University, West Lafayette, IN 47907; [b]Climate and Global Dynamics Laboratory, National Center for Atmospheric Research, Boulder, CO 80307; [c]School of Marine and Atmospheric Sciences, Stony Brook University, Stony Brook, NY 11794; and [d]Department of Atmospheric Science, Colorado State University, Fort Collins, CO 80521

Author contributions: F.L., D.R.C., B.M., and K.A.R. designed research; F.L. performed research; F.L., D.R.C., B.M., K.A.R., and K.L.R. analyzed data; and F.L., D.R.C., B.M., K.A.R., and K.L.R. wrote the paper.

The authors declare no competing interest.

This article is a PNAS Direct Submission.

[1]To whom correspondence may be addressed. Email: lifuning1991@gmail.com.

[2]Present address: Department of Earth, Atmospheric, and Planetary Sciences, Massachusetts Institute of Technology, Cambridge, MA 02139.

This article contains supporting information online at https://www.pnas.org/lookup/suppl/doi:10.1073/pnas.2315425121/-/DCSupplemental.

Published June 18, 2024.

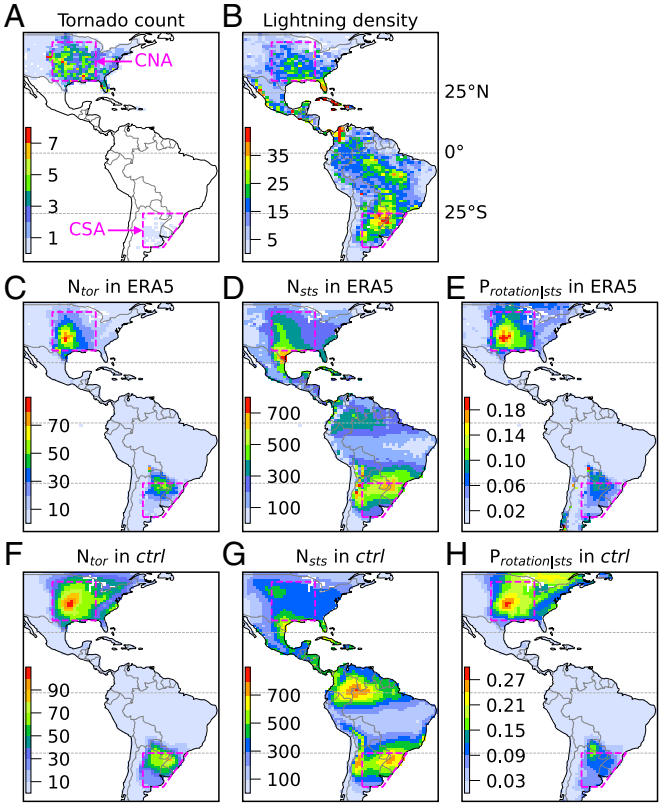

Fig. 1. CSA has lower tornado potential than CNA due to lower near-ground rotation potential. Dashed boxes represent the region of CNA and CSA. (*A*), Annual mean tornado density (counts year^{-1} per unit grid) for 1985 to 2014 at grid spacing of 1° (latitude) by 1.25° (longitude). (*B*), Annual mean lightning density (counts km^{-2} year^{-1}) for 1995 to 2010 from observations at grid spacing of 1° by 1.5°. (*C*–*E*), Annual mean N_{tor} (hours year^{-1}), N_{sts} (hours year^{-1}), and $P_{rotation|sts}$ from ERA5 reanalysis data for 1985 to 2014 at grid spacing of 1° by 1.25°. Quantitative relation refers to Eq. **1**. (*F*–*H*), As in (*C*–*E*) but from *ctrl* at grid spacing of 0.9° by 1.25°.

flow aloft (60). These air currents conspire to create environments favorable for severe thunderstorms and tornadoes (42, 61, 62).

A similar geographic setup is also found in South America, where the Andes Mountains stretch from north to south similar to the Rockies and Sierra Madre mountains, and the Amazon basin is as warm and moist as tropical oceans [colors in *SI Appendix*, Fig. S1 *A* and *B*; (63, 64)]. The Andes drive the climatological northerly low-level flow, within which is embedded a particularly strong flow feature commonly referred to as the South American low-level jet [SALLJ; (65–67)]. Similar to the Great Plains, strong northerly low-level flow is present east of the Andes as well; this feature is also enhanced synoptically by the passage of troughs [e.g., the northwestern Argentinean low and the Chaco low; (68–70)]. These northerly low-level winds transport warm and moist near-surface air from the upstream Amazon basin and tropical Atlantic Ocean into central South America [CSA; denoted by the box in Fig. 1*A*; (65, 66, 71–74)] to produce conducive environments for severe convection (75–80). Indeed, spaceborne radar and other remote sensing observations have shown that severe thunderstorms are more frequent (Fig. 1*B*) and extend to greater heights in CSA compared to CNA (81–83). However, tornado potential is substantially lower in CSA (10, 27), and relatively few major tornadoes have been reported in CSA, in stark contrast to CNA where there is a long history of devastating events [Fig. 1*A*; (30–34, 84)]. While storm reporting in CNA is mature and represents a relatively robust database, storm reports in CSA are not routinely available in a centralized database until very recently (32, 33, 84–86). Despite these large disparities in observational practices, the contrast between CNA and CSA is so stark that it is unlikely to be due to differences in reporting practices alone, though precise comparisons in tornado frequency between these two regions should be interpreted with caution (32, 33, 84, 85).

A recent South American severe thunderstorm field campaign (RELAMPAGO-CACTI) demonstrated that environments along the eastern edge of the Andes in CSA possess large values of the supercell composite parameter (SCP) and significant hail parameter (SHIP) and hence are conducive to severe storms and large hail (76). However, they were found not favorable for tornadoes primarily owing to relatively weak near-ground (0 to 1 km) vertical wind shear that causes low values of significant tornado parameter [STP; (76, 87, 88)], corroborating recent work using observations and reanalysis data (62, 84, 85, 89). In both CNA and CSA, a dominant source of low-level vertical wind shear is the poleward LLJ over each continent (7, 68, 71, 90–94). The vertical structure (e.g., peak height) differs between GPLLJ and SALLJ, as the Andes are in general taller and steeper than the Rockies such that slope effects are minimized while deeper lee cyclones develop near the Andes that help drive the SALLJ (67, 68, 71, 75, 88, 95–97).

One geographic contrast between CNA and CSA that has not yet been considered is that the tropical South American landmass is very rough due to land cover (e.g., Amazon rainforest roughness length $z_{0m} \sim 1$ m) and variable terrain (e.g., the Eastern Highlands), compared to the smooth and flat tropical ocean surface equatorward of North America (the Gulf of Mexico and Caribbean Sea; $z_{0m} \sim 10^{-4}$ m) (98, 99). Small-scale land surface roughness has been shown to reduce tornado formation locally (100). A modest reduction of the Amazon surface roughness by deforestation has been shown to intensify near-surface poleward winds and moisture transport along the climatological path of SALLJ (101). A modest modification of large-scale surface roughness has been shown to affect local mean wind speed over a deep layer up to 2.5 km above the ground surface (102). However, the role of large-scale upstream surface roughness, due to land cover and variable terrain, in modulating tornado activity downstream is unknown.

We hypothesize that the rough tropical South American landmass, compared to the smooth, flat tropical ocean surface equatorward of eastern North America, suppresses tornado potential downstream over CSA. A rough upstream land surface is expected to weaken poleward low-level winds, including the LLJ, that flow downstream to help produce tornadic environments. We first test this hypothesis in two ways to demonstrate this effect using global climate model (GCM) experiments: i) with the tropical South American land surface smoothed and flattened to be ocean-like; and ii) with the Gulf of Mexico and Caribbean Sea surface roughened to values comparable to a forested flat land, respectively. We then show that this result holds for an arbitrary midlatitude landmass using aquaplanet (i.e., an ocean-covered Earth) GCM experiments with an idealized continent and mountain range with a smooth versus rough equatorward ocean surface.

We define tornado potential, N_{tor}, as the mean frequency of tornadic environments per unit area and per year or per season. As a tornado typically forms from a preexisting severe thunderstorm as described above, we decompose tornado potential as the product of the severe thunderstorm potential (mean frequency of severe thunderstorm environments per unit area and per year or per season), N_{sts}, and a conditional probability of strong near-ground rotation potential (SRH01) given the existence of a severe thunderstorm environment, $P_{rotation|sts}$:

$$N_{tor} = N_{sts} P_{rotation|sts}. \quad [1]$$

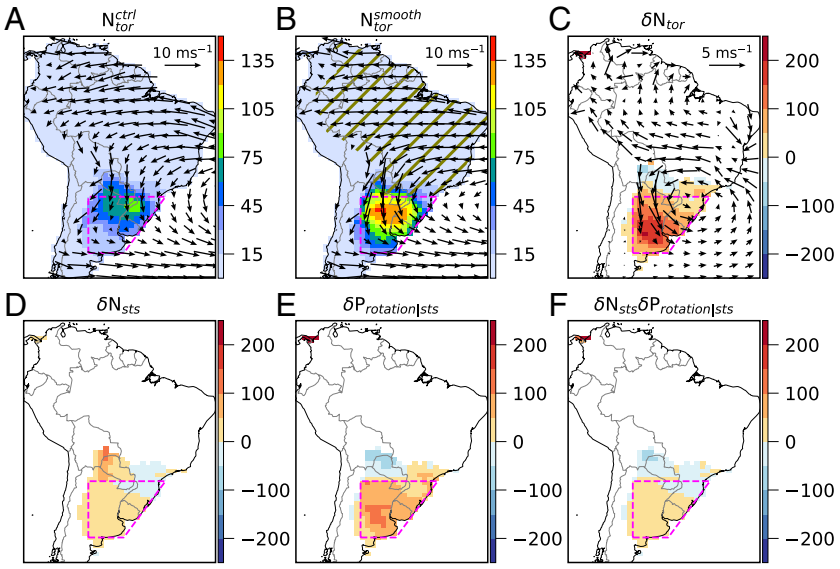

Fig. 2. A smooth, flat ocean-like upstream land surface enhances tornado potential downstream over CSA. (*A* and *B*), Annual mean N_{tor} (hours year^{-1}) with 850-hPa wind vectors (m s^{-1}) overlaid from *ctrl* (*A*) and *smooth* (*B*) for 1985 to 2014. 850 hPa is representative of the height of SALLJ. Dashed box indicates CSA. Hatched area in (*B*) indicates the upstream region modified in the experiment. (*C*), Relative changes [%] of N_{tor} in *smooth* with respect to *ctrl* with vectors representing differences in 850-hPa winds. (*D*–*F*), Relative changes [%] of N_{sts} (*D*), $P_{rotation|sts}$ (*E*), and their interaction term (*F*). Variables are defined following Eq. **2**. Note the different wind vector scale in (*A* and *B*) vs. (*C*). For full details of the experimental setup, the reader is referred to the *Materials and Methods*.

Therefore, relative changes in N_{tor} are explained by the sum of relative changes in N_{sts} and $P_{rotation|sts}$ and their interaction term:

$$\delta N_{tor} = \delta N_{sts} + \delta P_{rotation|sts} + \delta N_{sts}\delta P_{rotation|sts}. \quad [2]$$

Using ERA5 historical reanalysis data for 1985 to 2014 (103), we first confirm that tornado potential is substantially lower in CSA as compared to CNA (Fig. 1*C*), consistent with observed tornado activity [Fig. 1*A*;]. This contrast is not driven by severe thunderstorm potential, as annual N_{sts} is actually slightly larger in CSA than in CNA (Fig. 1*D*), similar to observed lightning activity [Fig. 1*B*;]. Instead, this contrast is driven by the near-ground rotation potential, with an annual domain-mean $P_{rotation|sts}$ that is twice as large in CNA as in CSA (Fig. 1*E*).

We conduct GCM experiments using the CESM2.1.1 (104) to test our hypothesis that the contrast in tornado potential between CSA and CNA is caused by the strong roughness of the land surface upstream of CSA relative to the smooth, flat ocean surface upstream of CNA. The control simulation (denoted as *ctrl*) is a historical global climate simulation during 1985 to 2014. In general, *ctrl* quantitatively reproduces the lower magnitude of N_{tor} in CSA than in CNA (Fig. 1*F*). This difference is driven principally by a much smaller $P_{rotation|sts}$ (Fig. 1*H*) rather than a difference in N_{sts} (Fig. 1*G*). The similarity in the frequency of severe thunderstorm environments between CSA and CNA extends to extreme CAPE and S06 themselves in both ERA5 and *ctrl*. The *ctrl* also produces a realistic distribution of the low-level winds as compared to ERA5, including the seasonal cycle of 850-hPa winds (vectors in *SI Appendix*, Fig. S1 *A* and *B*) and the diurnal cycle of the frequency and intensity of LLJ within CSA and CNA (*SI Appendix*, Fig. S1 *C* and *D*; detailed in *Materials and Methods*.

We first show that our hypothesis is supported by comparing *ctrl* against an experiment in which the tropical South American landmass is smoothed and flattened to be ocean-like [denoted as *smooth*; *SI Appendix*, Fig. S2 *A*–*H*;]. The change to an ocean-like surface upstream substantially increases tornado potential downstream over CSA (Fig. 2 *A* and *B*). Relative to *ctrl*, annual N_{tor} in *smooth* increases by up to +203% particularly over northeastern Argentina (Fig. 2*C*). Experiments deconstructing contributions from upstream land cover, resolved terrain, and parameterized elevation roughness demonstrate that the responses are driven approximately equally by the land cover (*SI Appendix*, Fig. S5*A*) and resolved terrain (*SI Appendix*, Fig. S5*B*), and to a lesser extent by the parameterized elevation roughness (*SI Appendix*, Fig. S5*C*).

The increase in CSA tornado potential in *smooth* is driven principally by the increase of up to +115% in $P_{rotation|sts}$ (Fig. 2*E*), while N_{sts} (Fig. 2*D*) and the interaction term (Fig. 2*F*) increase modestly (+42% and +46%). These responses are associated with enhanced easterly winds at 850 hPa over the upstream surface due to the reduced upstream surface resistance to the flow in *smooth*. Through the mechanical forcing (45, 46) of the Andes (65–67), the stronger easterly trade winds lead to stronger northerly mean winds flowing downstream along the eastern slope of the central Andes into CSA at 850 hPa (vectors in Fig. 2*C*). This induces an anticyclonic anomaly at 850 hPa that enhances the South American Subtropical High. Such a strong enhancement of N_{tor} and northerly low-level flow within CSA is found in all seasons (*SI Appendix*, Fig. S3). Associated with this strong mean flow response at 850 hPa which is extended to severe thunderstorm environments, the conditional low-level vertical wind shear from the surface to 1 km above increases over CSA (thick curves in *SI Appendix*, Fig. S4*A*), which is the principal driver of the increase in SRH01 that produces environments more favorable to tornadoes within CSA in *smooth*. The modest increase in severe thunderstorm potential is driven by an increase in low-level moisture below 4 km (*SI Appendix*, Fig. S4*B*), likely associated with enhanced moisture transport from the South Atlantic Ocean by the intensified easterlies upstream and northerly flow downstream that generates thermodynamic environments more favorable to convection. These results are consistent with a strong increase in the frequency of SALLJ within CSA, especially during the afternoon (*SI Appendix*, Fig. S4*C*), as well as the enhanced intensity of SALLJ throughout the day (*SI Appendix*, Fig. S4*D*). These results provide evidence that the rough equatorward land surface of South America due to (surface roughness and terrain), in contrast to a smooth and flat ocean surface, strongly suppresses central South American tornado potential primarily by reducing near-ground rotation

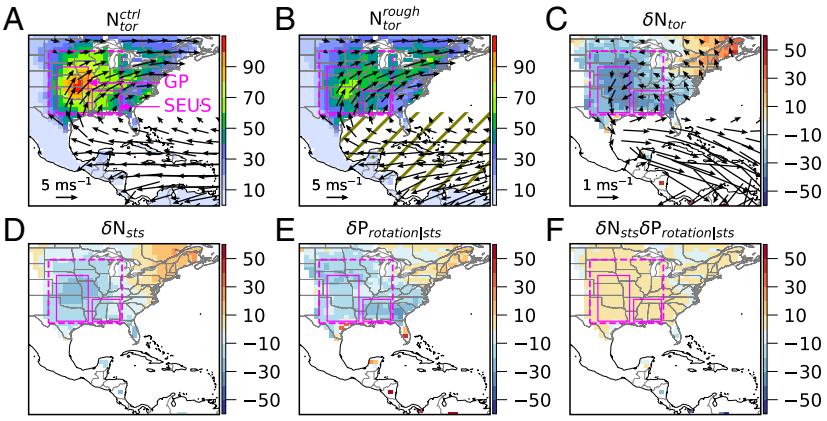

Fig. 3. A roughened upstream ocean surface suppresses tornado potential downstream over CNA. (*A–F*), As in Fig. 2, but for *ctrl* versus *rough* with wind vectors at 925 hPa, representative of the height of GPLLJ. Dashed box indicates CNA. Two small boxes within CNA indicate the Great Plains (GP) and the Southeast United States (SEUS). Hatched area in (*B*) indicates the upstream region modified in the experiment. Note the different wind vector scale in (*A* and *B*) vs. (*C*). For full details of the experimental setup, the reader is referred to the *Materials and Methods*.

potential, and secondarily by reducing severe thunderstorm potential.

While we focus on the upstream surface impact on the downstream region in this work, we note a contrasting response locally over the upstream surface: The stronger inland intrusion of the easterlies from the subtropical South Atlantic Ocean in *smooth*, deflected by the central Andes, induces a weakened northerly mean flow at 850 hPa over northern Bolivia and Peru (vectors in Fig. 2*C*). This is primarily due to the flattened terrain (vectors in *SI Appendix*, Fig. S5*B*), though the reduced land-cover roughness itself favors stronger easterlies over the Amazon basin and hence a stronger northerly flow over northern Bolivia [vectors in *SI Appendix*, Fig. S5*A*; (101)]. This results in transient responses locally over Bolivia-Paraguay with N_{sts} increases (Fig. 2*D*) but $P_{rotation|sts}$ decreases (Fig. 2*E*). The decrease in local $P_{rotation|sts}$ is consistent with the decrease in low-level vertical wind shear over the upstream (local) surface [thin curves in *SI Appendix*, Fig. S4*A*;]. How tropical land-cover roughness and tropical terrain resistance, and their interaction, might modulate severe weather activity locally over Northern South America is a topic worthy of future work.

Additional analyses and GCM experiments add robustness to the result in *smooth*. The robust response of N_{tor} within CSA in *smooth* is consistent for any desired thresholds defining severe thunderstorm and tornadic environments (*SI Appendix*, Figs. S9 *A–D* and S10 *A–E*; detailed in *Materials and Methods*. While the land cover determines both the surface momentum roughness (z_{0m}) and enthalpy roughness (z_{0k}), an experiment with z_{0k} fixed produces only a slightly stronger response of N_{tor} than *smooth*, showing that z_{0m} is the dominant driver as compared to z_{0k} (*SI Appendix*, Fig. S5*D*). Smoothing and flattening a smaller area of the upstream surface also produces a strong response in N_{tor}, but it is smaller than in *smooth* (*SI Appendix*, Fig. S5*E*). This indicates that the magnitude of this response depends on the area of the upstream surface, though the upstream surface closer to CSA appears to have a larger effect than the upstream surface farther from CSA.

We next show that our hypothesis is also supported by comparing *ctrl* against an experiment in which the upstream equatorward ocean surface of North America is roughened to be as rough as a rainforest-covered flat land surface (denoted as *rough*; in *Materials and Methods*). For simplicity, flow resistance due to variable terrain is not considered. The change to a rough ocean surface upstream substantially suppresses the tornado potential downstream over CNA (Fig. 3 *A* and *B*). Relative to *ctrl*, annual N_{tor} in *rough* decreases by up to −41% (i.e., an increase of +70% in *ctrl* relative to *rough*), particularly over the Great Plains and the Southeast United States (Fig. 3*C*).

In contrast to CSA, the response in N_{tor} is driven by the decrease in both N_{sts} (up to −30%; Fig. 3*D*) and $P_{rotation|sts}$ (up to −27%; Fig. 3*E*), with a negligible increase from the interaction term (up to +5%; Fig. 3*F*). These relative changes vary by region, as the decrease of $P_{rotation|sts}$ is a larger driver over the Southeast United States while the decrease of N_{sts} is a slightly larger driver over the Great Plains. Over the Great Plains, the response is again associated with weakened easterly winds at 925 hPa over the roughened ocean surface in *rough*, driving weakened southerly winds at 925 hPa flowing downstream into the Great Plains (vectors in Fig. 3*C*) through the mechanical forcing of the Rockies (45, 46). Such a weakening of N_{tor} and southerly low-level flow over the Great Plains is found in all seasons (*SI Appendix*, Fig. S6). In this case, the low-level vertical wind shear from the surface to 1 km conditioned on severe thunderstorm environments decreases over the Great Plains (thick lines in *SI Appendix*, Fig. S4*E*) as does the low-level moisture below 2 km in the mean state (*SI Appendix*, Fig. S4*F*). These results are consistent with the reduced frequency of LLJ, especially during the late afternoon (*SI Appendix*, Fig. S4*G*), though the weakening of LLJ intensity is relatively minor (*SI Appendix*, Fig. S4*H*). Meanwhile, over the Southeast United States, the conditional low-level shear (thick lines in *SI Appendix*, Fig. S4*I*) and mean-state moisture (*SI Appendix*, Fig. S4*J*) also decrease by similar magnitudes to the Great Plains, reflecting a weakened onshore flow within severe thunderstorm environments. This is consistent with the reduced LLJ intensity within this area (*SI Appendix*, Fig. S4*L*) and the reduced LLJ frequency during the afternoon, though the nocturnal LLJ frequency slightly increases (*SI Appendix*, Fig. S4*K*). In this region the mean-state onshore flow field at 925-hPa is actually slightly enhanced in *rough* (vectors in Fig. 3*C*). Hence, the low-level shear response over the Southeast United States is transient, occurring within severe thunderstorm environments but not in the mean state.

Additional analyses and GCM experiments also add robustness to the result in *rough*. Such a strong response of N_{tor} holds for any desired thresholds defining severe thunderstorm and tornadic environments (*SI Appendix*, Figs. S9 *E–H* and S10 *F–J*; detailed in *Materials and Methods*. Roughening a smaller area of the upstream surface (i.e., the Gulf of Mexico only) also produces a strong response but is smaller than in *rough* (*SI Appendix*, Fig. S7*A*), again indicating the dependence of the response on the area of the upstream surface.

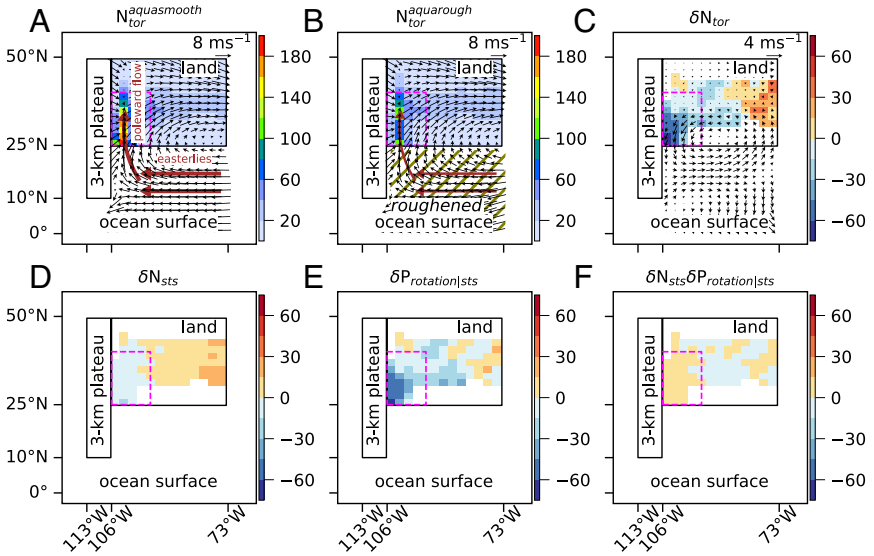

Fig. 4. A rougher upstream ocean surface suppresses downstream tornado potential in idealized aquaplanet GCM experiments, too. (*A–F*), As in Fig. 2, but for *aquasmooth* versus *aquarough* with vectors representing 850-hPa winds. Hatched area in (*B*) indicates the upstream region modified in the experiment. Note the different wind vector scale in (*A* and *B*) vs. (*C*). For full details of the experimental setup, the reader is referred to the *Materials and Methods*.

These results for North America are qualitatively consistent with the results of South America above, suggesting that the strong contrast in upstream surface roughness and terrain drives the marked contrast in the climatology of tornado activity between the two continents. The spatial pattern and drivers are a bit more complex, with the thermodynamic response playing a more significant role in CNA than CSA. The Great Plains response is similar to CSA via the role of the poleward low-level flow and the LLJ within it, whereas the response in the Southeast United States differs in its transient mechanism. This reflects the well-known contrast in the behavior of tornado activity between the two subregions (15, 39, 40, 105, 106). The responses in North America are overall smaller in magnitude than in South America above, perhaps because there is no experimental analog in *rough* for the influence of the upstream highlands, which was shown to be as important as land cover roughness in *smooth* (*SI Appendix*, Fig. S5 *A* and *B*). Other topographic differences between these two continents, such as the height (66, 75, 95, 107) and slope (47, 51) of the Rockies versus the Andes that drive differences in the mechanisms of LLJ formation, may also modulate regional severe weather activity differently. In addition, the wider extent of the Rockies may favor more elevated mixed layers and drylines that are more favorable to the formation of severe thunderstorm and tornadic environments over North America (62, 108).

Finally, we show that our hypothesis is supported more generally for a midlatitude landmass poleward of a tropical ocean on an Earthlike planet, using idealized aquaplanet GCM experiments (109–111). We design a smooth aquaplanet simulation (denoted as *aquasmooth*) that contains the minimal geographic ingredients for severe thunderstorm environments (42). The setup has an idealized rectangular midlatitude continent with a 3 km north–south oriented plateau along its western edge (Fig. 4*A*). This height is between the height of the Rockies and Andes. For simplicity, the plateau is narrow (7.5 degrees of longitude) and steep (a slope of 90 degrees) and thus is similar to the shape of the Andes. The *aquasmooth* successfully reproduces a "tornado alley"-like region of significant tornado potential east of the plateau (Fig. 4*A*) with a strong seasonal cycle that peaks in springtime (*SI Appendix*, Fig. S8). To test our hypothesis, we compare *aquasmooth* with a rough aquaplanet experiment in which the surface roughness of the tropical ocean equatorward of the continent is enhanced to be analogous to the roughness magnitude of the rainforest-covered flat land surface (denoted as *aquarough*; Fig. 4*B*; *Materials and Methods*).

The aquaplanet results support our hypothesis, as annual tornado potential within the tornado region in *aquarough* is strongly suppressed by up to −67% relative to *aquasmooth* (i.e., an increase of +203% in *aquasmooth* relative to *aquarough*; Fig. 4*C*). This response is driven principally by the decrease in $P_{rotation|sts}$ (~ −60%; Fig. 4*E*) with a small contribution from the decrease in N_{sts} (~ −14%; Fig. 4*D*) and a small increase due to the interaction term (+7%; Fig. 4*F*). Similar to the real-world GCM experiments above, particularly South America, these responses are associated with weakened easterly winds at 850 hPa over the upstream roughened ocean surface in *aquarough*, which thus weakens the southerly winds flowing downstream into the continental interior (vectors in Fig. 4*C*). Such a strong weakening of N_{tor} and southerly low-level flow within the continental interior is found in all seasons (*SI Appendix*, Fig. S8). The weakened low-level (850 hPa) winds primarily reduce the conditional low-level vertical wind shear from the surface to 1 km above (thick lines in *SI Appendix*, Fig. S4*M*), and the inland moisture transport in the lower troposphere below 4 km (*SI Appendix*, Fig. S4*N*), and thereby produces environments less favorable to tornadoes. This result is consistent with a decrease in the frequency and intensity of LLJ throughout the day (*SI Appendix*, Fig. S4 *O–P*). We note that *aquasmooth* does not produce an obvious coastal region of elevated tornado potential farther east that would be analogous to the Southeast United States, a topic worthy of future research. Nonetheless, this outcome again highlights the contrast in storm behavior between the Southeast United States and the Great Plains (15, 39, 40, 105, 106).

These strong responses in *aquarough* are again robust to any desired thresholds defining severe thunderstorm and tornadic environments (*SI Appendix*, Figs. S9 *I–L* and S10 *K–O*; detailed in *Materials and Methods*. Finally, results are not specific to the magnitude of roughening, as the response increases as the upstream surface is more strongly roughened (*SI Appendix*, Fig. S7 *B* and *C*. This is consistent with the finding that the response over CSA in *smooth* is stronger than that over CNA in *rough* due to the complex terrain over the tropical South America (e.g., the presence of the Eastern Highlands), which causes a rougher tropical South American landmass than the roughened tropical ocean surface in *rough* (112).

This work adds a critical missing ingredient to our conceptual understanding of the geographic controls of tornado hotspots on Earth: a smooth, flat ocean-like upstream surface. A smoother upstream surface permits stronger easterly trade winds that feed the poleward low-level winds flowing downstream into the continental interior (red arrows in Fig. 4 *A* and *B*). Despite mechanistic and structural differences between the continents, the poleward low-level winds, including the GPLLJ over central North America and SALLJ over central South America, help generate the strong near-ground environmental vertical wind shear necessary for tornadoes and also enhance inland moisture transport. Our real-Earth and idealized global climate model experiments successfully capture such direct impacts of the large-scale upstream surface roughness on the geography of tornado potential over both continents. Our analyses indicate that a smooth, flat ocean surface upstream, as compared to a rougher land, is ideal for generating a regional tornado hotspot as found in central North America. The rainforest cover and terrain complexity further enhance the roughness of the tropical South American landmass. If the tropical South American land surface were less rough (i.e., more ocean-like), tornado potential over central South America might be more similar to that found over central North America (Fig. 2*B* versus Fig. 3*A*).

Here, we have focused on the role of *continental-scale* roughness *upstream* of the severe weather regions of North America and South America. Note that the wind hodograph influenced by surface roughness is not simply passively advected downstream from the modified upstream region. Previous studies have indicated that the local air parcels associated with convective environments over CNA originate from distinct upstream locations at each level (57, 113). This is also true in our experiments for both CNA and CSA (*SI Appendix*, Fig. S11), as changes in the local wind speed and direction at each level imply changes in the source location of parcels at those levels. Modifying the continental-scale upstream surface roughness slightly modifies the inflow trajectory of the parcels that ultimately comprise the low-level wind profiles locally over CNA or CSA, though they still originate over the same broad regions upstream. We hope that this work will open up research questions regarding how regional heterogeneity of topography and the land surface (land cover and variable terrain) can modify regional tornado activity, both downstream and locally, as well as the role of higher resolution topographic and land-surface interactions with low-level winds and boundary-layer processes that could be tackled in future work (97, 102, 114). This includes the emergence of the South American Eastern Highlands and the Amazon rainforest basin in paleoclimate records (115), and Amazonian deforestation and regional land cover changes in the eastern half of the United States in the modern climate (101, 116). Moreover, an important question is how terrain and land cover may alter the response of tornadoes in the future, as climate change may -modulate the large-scale atmospheric circulation and the geographic patterns of severe thunderstorm and tornado activity that it produces (106).

While upstream surface roughness and terrain appear to play a first-order role in the contrast of tornadic environments between North and South America, there certainly may be other factors that also contribute to the contrast in tornadic environments and in tornado activity between the two continents. We hope our study motivates future research exploring those additional factors. This includes differences in other geographic properties, such as the mountain and landmass orientation and extent (47, 66, 75, 84, 95, 107, 117), which may shift the central latitude of the tornado hotspot and hence interact with large-scale environments differently (e.g., mid-latitude storm tracks). Moreover, we have focused on tornado potential based on the widely used set of necessary ingredients for tornadogenesis, yet tornadoes themselves are especially complex. Differences in other, less well-understood storm-scale factors that have been found to influence tornadogenesis [e.g., updraft width, cold pool, and convective modes; (118–120)] may also differ in storms over the two continents. Future work researching these questions may seek to employ high-resolution modeling experiments [e.g., storm-resolving models and large-eddy simulations; (121–125)] to explicitly resolve these processes, as well as to consider recent theoretical advances in environmental controls of the formation of severe thunderstorms and tornadoes [e.g., entraining CAPE and storm relative helicity components; (126, 127)] once they are incorporated into environmental proxies that become standard in the forecasting community.

Materials and Methods

Tornadic Environments and Tornado Potential. We define a severe thunderstorm environment to have convective available potential energy (CAPE; a measure of atmospheric instability) and 0 to 6 km bulk wind difference (S06; a measure of deep-layer vertical wind shear) each exceeding a specified lower-bound threshold. Tornadic environments are defined as severe thunderstorm environments that additionally have 0 to 1 km storm relative helicity (SRH01, a measure of the potential for a near-ground air parcel to generate rotation as it flows into the base of a storm) exceeding a specified lower-bound threshold. Following past work, we initially set these thresholds to 150 J kg^{-1} for CAPE, 10 m s^{-1} for S06 (14, 16, 17), and 200 m^2 s^{-2} for SRH01 (19, 20, 22, 24, 25), respectively. These thresholds for CAPE and S06 are close to the lower bounds of CAPE and S06, above which most tornadoes occur across the contiguous United States (14, 22, 25, 128). This enables the inclusion of low-CAPE tornadic environments that are commonly found for tornadoes over the Southeast United States and during cool seasons (*SI Appendix*, Fig. S6*D*), which account for a significant portion of all tornadoes across the contiguous United States (22, 105, 128). The threshold for SRH01 is close to the lower 25th percentile SRH01 for significant (EF2+) tornadoes and median SRH01 for weaker tornadoes but the 90th percentile SRH01 for nontornadic severe thunderstorms across the contiguous United States (22); hence, it ensures a relatively high possibility for producing tornadoes from preexisting severe thunderstorms. We show below that our results are robust to any desired thresholds.

We define tornado potential (N_{tor}) as the mean frequency of tornadic environments per unit area and per year or season and severe thunderstorm potential (N_{sts}) as the mean frequency of severe thunderstorm environments per unit area and per year or season. The conditional probability of strong near-ground rotation potential ($P_{rotation|sts}$) is the probability of SRH01 exceeding 200 m^2 s^{-2} in magnitude (favorable SRH01 is positive in the Northern Hemisphere and negative in the Southern Hemisphere) conditioned on the existence of severe thunderstorm environments.

Specifically, CAPE is defined as the vertical integral of positive buoyancy between the level of free convection (z_{LFC}) and the equilibrium level (z_{EL}) of a hypothetical mixed-layer air parcel lifted from near the surface (43), Eq. **3**, where g is the acceleration due to gravity. We define mixed layer as the lowest 500 m above the surface, consistent with (14, 16–18). S06 represents lower-tropospheric environmental horizontal vorticity, defined as the absolute magnitude of the wind vector difference between 6 km ($\mathbf{V}_{6km}$) and 10 m ($\mathbf{V}_{10m}$) above the surface (10), Eq. **4**, SRH01 represents the streamwise (in the Northern Hemisphere) or anti-streamwise (in the Southern Hemisphere) horizontal vorticity of the 0 to 1 km environmental flow parallel to the storm inflow direction, which measures the potential for near-ground updraft rotation needed for tornado formation (19, 20, 22, 24–26), Eq. **5**, where $\mathbf{V}$ is the height-varying wind vector from 10 m to 1 km above the surface, $\mathbf{V}_s$ is the storm motion vector (129), and $\hat{\boldsymbol{k}}$ is the vertical unit vector. We use the greater absolute value of SRH01 between the right- and left-moving storms for each time step and grid point so that it is valid for both the Northern and Southern Hemisphere (18).

$$\mathrm{CAPE} = \int_{z_{LFC}}^{z_{EL}} g \frac{T_{vp} - T_{ve}}{T_{ve}} dz, \qquad [3]$$

$$S06 = \left|\boldsymbol{V}_{6\mathrm{km}} - \boldsymbol{V}_{10\mathrm{m}}\right|, \quad [4]$$

$$\mathrm{SRH01} = -\int_{z=10\mathrm{m}}^{z=1\mathrm{km}} \hat{\boldsymbol{k}} \cdot \left(\boldsymbol{V} - \boldsymbol{V}_s\right) \times \frac{\partial \boldsymbol{V}}{\partial z} dz. \quad [5]$$

We calculate CAPE and SRH01 using the *xcape* python package (18), publicly available at https://github.com/xgcm/xcape. We use the vertical linear interpolation of the *interpolate_to_isosurface* function within the *metpy* package (130), publicly available at https://github.com/Unidata/MetPy, to obtain winds at 6 km above the surface for calculating S06.

Robust to Thresholds and Proxies. While the performance of environmental proxies in representing severe thunderstorm and tornado potential varies by season and region (22, 131), which poses challenges for choosing threshold values for environmental proxies (17), we show that our results (responses across experiments) are robust to any combinations and specific values of thresholds of these parameters (*SI Appendix*, Figs. S9 and S10), as well as to the addition of other key parameters such as the convective inhibition (CIN) and significant tornado parameter (STP) (*SI Appendix*, Fig. S10).

First, our conclusions are not sensitive to the thresholds for defining severe thunderstorm environments, as we detect a robust decrease in tornado potential in *rough* (relative to *ctrl*; *SI Appendix*, Fig. S9 *E–G*) and a robust increase in *smooth* (relative to *ctrl*; *SI Appendix*, Fig. S9 *A–C*)and *aquasmooth* (relative to *aquarough*; *SI Appendix*; Fig. S9 *I–K*) across a wide range of lower-bound thresholds for CAPE and S06. Similarly, our conclusions are not sensitive to the threshold for defining rotation potential, as we detect a robust decrease in tornado potential in *rough* (*SI Appendix*, Fig. S9*H*) and a robust increase in *smooth* (*SI Appendix*, Fig. S9*D*) and *aquasmooth* (*SI Appendix*, Fig. S9*L*) for any threshold values of SRH01, and the percentage responses are larger for larger SRH01 thresholds. Second, in addition to the low CAPE and S06 thresholds and high SRH01 threshold used in the main text, we further test combinations of 1) low CAPE and S06 thresholds and low SRH01 threshold (*SI Appendix*, Fig. S10 *A*, *F*, and *K*), 2) high CAPE and S06 thresholds and high SRH01 threshold (*SI Appendix*, Fig. S10 *B*, *G*, and *L*), and 3) high CAPE and S06 thresholds and low SRH01 threshold (*SI Appendix*, Fig. S10 *C*, *H*, and *M*) to show that the responses across experiments are very similar across all combinations of low/high thresholds of CAPE, S06, and SRH01. The high thresholds of CAPE and S06 yield CAPE×S06 $>4 \times 10^4$, which are most commonly associated with severe thunderstorms and tornadoes over the Great Plains and during warm seasons when high-CAPE and high-S06 environments are more favorable (12, 15, 22, 90); indeed, observations indicate that over 50% of right-moving supercell EF2+ tornadoes in the contiguous United States occurred when CAPE $>$ 1,519 J kg^{-1} and S06 $>$ 30 m s^{-1} [1,519 × 30 = 45,570; (22)]. Third, we show that the results are robust to the addition of a threshold on CIN > -125 J kg^{-1}. [*SI Appendix*, Fig. S10 *D*, *I*, and *N*; (18)]. A low CIN represents a low potential energy barrier that external forcing must overcome to initiate deep convection, which is more representative of tornadic environments over southern Brazil (7, 91, 92) and the Southeast United States (39, 40). Last, we test quantifying tornado potential by STP $>$ 1 (20, 24, 25) and show that the results are robust (*SI Appendix*, Fig. S10 *E*, *J*, and *O*). STP is a commonly used forecasting tornado index by the Storm Prediction Center. We follow past work to define STP (20) based on CAPE, SRH01, S06, and lifting condensation level (LCL).

Overall, though detailed regional patterns and absolute values of tornado potential vary with these modified environmental proxies and thresholds, they do not change the finding that the strong responses of tornado potential to upstream surface roughness in all of our experiments hold for these modified definitions.

Observation and Reanalysis Datasets. Observed EF0+ tornado records in the United States during 1985 to 2014 are obtained from the Storm Prediction Center (https://www.spc.noaa.gov/wcm/). A validated dataset for tornado reports over the southeastern South America during 1991 to 2020 is publicly available at https://doi.org/10.5281/zenodo.7072781 (132) and is described in more detail in ref. 84. Note that this database includes only tornado reports that could be independently verified (i.e., photographic evidence or corresponding newspaper reports from the region) and does not include all available tornado reports. Thus, the number of tornadoes is likely significantly underestimated, especially for some tornadoes reported over the southeastern Brazil (33, 85, 91, 92). Caution should be exercised in directly comparing the frequency of tornado reports in CNA and CSA, though the stark qualitative contrast between the two regions is likely to be robust. Future efforts are needed to correct reporting biases (133) and build up a long-term database for South American tornado activity by incorporating all available and verified data sources, which may help to perform a quantitative applies-to-applies comparison of tornado activity between CNA and CSA. Counts of EF0+ tornadoes in the United States and all verified tornadoes over the southeastern South America are used to generate Fig. 1*A*. We do not condition on EF0+ tornadoes for South America because over 60% of these tornadoes do not report accurate intensities (84), though the stark contrast between CNA and CSA is still evident for EF0+ or higher-intensity tornadoes.

Annual mean flash during 1995 to 2010 from 0.5° × 0.5° gridded climatological data of lightning flashes seen by the spaceborne optical transient detector (OTD) and Lightning Imaging Sensor (LIS) is used to generate Fig. 1*B*, obtained from https://ghrc.nsstc.nasa.gov/pub/lis/climatology/LIS-OTD/HRFC/data/nc/. Here, lightning density is used to approximate the climatology of severe thunderstorm activity in central North and South America, though in the tropics, it usually represents less severe storms where deep-layer wind shear is in general small.

The ERA5 reanalysis (103) has been shown to closely match in situ observations (e.g., radiosondes) of key convective environmental parameters (14, 15, 17, 25). We use the 3-hourly ERA5 data during the period 1985 to 2014 at 37 constant pressure levels from 1,000 to 1 hPa (7 levels between 1,000 and 850 hPa). The pressure-level data are interpolated from the original 137-model-level ERA5 data (103) and combined with the near-surface (10 m above ground surface) data. The horizontal grid spacing is 0.25 degrees. We obtain the dataset from NCAR's Research Data Archive, publicly available at https://doi.org/10.5065/BH6N-5N20.

Real-Earth GCM Experiments. We use the community atmosphere model version 6 (CAM6) coupled to the Community Land Model version 5 (CLM5), within the Community Earth System Model version 2.1.1 (CESM2.1.1) (104), to conduct the control historical simulation (denoted as *ctrl*), the South American experiment with modified equatorward land surface (denoted as *smooth*), and the North American experiment with modified equatorward ocean surface (denoted as *rough*). CESM2.1.1 model source code is publicly available at https://www.cesm.ucar.edu/models/cesm2/release_download.html.

The *ctrl* is the default FHIST component configuration within CESM2.1.1. It uses the finite-volume dynamical core, configured on a 0.9°× 1.25° latitude-longitude grid mesh with 32 hybrid sigma-pressure levels. There are 6 to 7 levels (vary by region) over the lowest 1 km above the surface. Historically annual changes in global natural and crop vegetation are considered in CLM5 by prescribing the annual transient land use and land cover data based on observations from 1979 to 2014. This helps produce reasonable surface roughness over canopy, as the surface roughness length is proportional to the height of vegetation (104). The global ocean is prescribed with monthly historical sea surface temperatures and ice coverage created from merged Hadley-NOAA/OI products (134). We integrate the simulation over the period 1979 to 2014 on NCAR's Cheyenne supercomputers, discard the first 6 y for spinup, and analyze the 3-hourly output from 1985 to 2014. Past work shows that a similar historical simulation using CESM2.1.0 successfully reproduces realistic climatology of severe convective storm environments in North America with similar spatial patterns, seasonal cycles, and diurnal cycles as compared to the ERA5 historical climatology (15). Similar to ref. 15, *ctrl* reasonably reproduces the climatological spatial patterns of severe thunderstorm and tornado potentials in the ERA5, particularly the strong contrast between CNA and CSA (Fig. 1 *F–H*). The lower horizontal and vertical resolutions of CESM as compared to ERA5 may partially contribute to the high bias in severe thunderstorm potential over tropical South America (Fig. 1*D* vs. Fig. 1*G*), which may be improved by using high-resolution GCMs in future work. For both CNA and CSA, the modest high bias in severe thunderstorm potential is associated with the high bias in CAPE (15); this overestimation of CAPE is commonly found in most CMIP6 global climate models, associated with overestimations in near-surface moist static energy (135).

The *ctrl* also reasonably captures the diurnal cycle of LLJ frequency and intensity over CNA and CSA (*SI Appendix*, Fig. S1*D*), as well as other synoptic-scale features (e.g., drylines, elevated mixed layer, and extratropical cyclones) key to severe convective environments (15), as compared to the ERA5 (*SI Appendix*, Fig. S1*C*). The LLJ within the Great Plains is more frequent and has a stronger diurnal cycle than that within CSA (*SI Appendix*, Fig. S1 *C* and *D*), consistent with observations (49, 136). Following (136), we identify a wind profile as a LLJ if it meets the following three criteria: i) wind speed displays a local maximum equal

to or greater than 12 m s^{-1} within the lowest 3,000 m above ground surface, ii) wind speed decreases by at least 6 m s^{-1} from the maximum speed to the first minimum found aloft or to the speed at 4,000 m above ground surface, whichever occurs first, and iii) the wind vector of the maximum speed has a southerly component over North America or a northerly component over South America. The first two criteria are the same as ref. 136. Though larger limits to the heights in (i) and (ii) were suggested for detecting SALLJ (68) and a lower limit to the height in (ii) was suggested for detecting GPLLJ (49), we have tested to ensure that these modifications of criteria have a relatively small influence on the climatology of LLJ from the ERA5 and *ctrl*. We add the third criterion as we focus on the poleward LLJ.

The *smooth* is the same as *ctrl* except that the tropical South American surface (the hatched area in Fig. 2*B*) is smoothed and flattened to be ocean-like. Specifically, *smooth* includes three modifications (*SI Appendix*, Fig. S2 *E–H*) with respect to *ctrl* (*SI Appendix*, Fig. S2 *A–D*). First, we reduce the momentum roughness length (z_{0m}) and enthalpy roughness (z_{0k}) over vegetation canopies of the equatorward land (landmass within 25°S–13°N, 81.5°W–34°W) to the magnitude of 10^{-4} m, similar to that of ocean surface (*SI Appendix*, Fig. S2*E* versus A). We reduce both z_{0m} and z_{0k} because they are both determined by vegetation types and the default model parameterization sets z_{0k} to be identical to z_{0m}. Second, we remove the elevation roughness associated with parameterized small-scale terrain variance by setting the SD of 10-min elevations (SGH) and the SD of elevations from 30 s to 10 min (SGH30) to zero, except over the majority of the Andes (surface height greater than 500 m) where values are not altered (*SI Appendix*, Fig. S2 *F–G* versus B–C). Third, we flatten the equatorward land surface itself by setting the surface elevation (z_{sfc}) to zero except over the Andes Mountains in the same manner as above (*SI Appendix*, Fig. S2*H* versus D). We choose 25°S, as it is approximately the northern boundary of the majority of central South American tornado activity (Fig. 1*A*), though some tornadoes are reported at lower latitudes of South America (33, 91, 92). Thus, the modified equatorward land in *smooth* creates an ocean-like smooth surface upstream of the tornado hotspot of central South America, similar to North America where the smooth equatorward ocean surface (i.e., the Gulf of Mexico and the Caribbean Sea) is located upstream of the tornado hotspot of central North America. To effectively test our hypothesis, our modifications in *smooth* relative to *ctrl* seek to isolate kinematic impacts of surface roughness and terrain. Though local surface latent heat flux is slightly reduced due to the reduction of z_{0m} and z_{0k}, this local thermal response has been minimized as we keep land cover types and soil properties unchanged. To help distinguish the individual role of each modification, we conduct additional three experiments with each modification applied individually (*SI Appendix*, Fig. S5 *A–C*). To test whether the influence of enthalpy roughness is strong, we conduct an additional experiment with the enthalpy roughness unchanged and otherwise the same as *smooth* (*SI Appendix*, Fig. S5*D*). We also conduct an additional experiment with a smaller region upstream of the central South America smoothed and flattened to determine whether the results depend on the area of the upstream surface modified (*SI Appendix*, Fig. S5*E*).

The *rough* is the same as *ctrl* except that the tropical North American ocean surface (the hatched area in Fig. 3*B* including the Gulf of Mexico and the Caribbean Sea) is roughened to be as rough as the rainforest-covered Amazon basin. Specifically, instead of modifying the surface momentum roughness length (z_{0m}) as in *smooth* above, here we enhance the drag coefficient (C_d) at the lowest model level (roughly 60 m above the surface) by a factor of 10. This is because the ocean module in the model does not explicitly solve for z_{0m} but does solve for C_d when calculating turbulence fluxes at the lowest model level. The empirical relation between C_d and z_{0m} is

$$C_d \approx \frac{k^2}{\left[\ln\left(\frac{z}{z_{0m}}\right)\right]^2}, \qquad [6]$$

where $k = 0.4$ and $z \approx 60$ m. Thus, we estimate $C_d \approx 0.9 \times 10^{-3}$ given $z_{0m} \approx 10^{-4}$ m for ocean and $C_d \approx 9.5 \times 10^{-3}$ given $z_{0m} \approx 1$ m for the Amazon surface [*SI Appendix*, Fig. S2*A*; (98, 99)]. This yields roughly a factor of 10 difference between the rough and smooth ocean surface. We also conduct an additional experiment with only the Gulf of Mexico surface modified to determine whether results depend on the area of the upstream surface modified (*SI Appendix*, Fig. S7*A*).

The momentum roughness length (z_{0m}) determines the magnitude of momentum flux exchange at the interface of Earth's surface and atmosphere (137). A large value of z_{0m} indicates large surface momentum flux exchanges and hence a large frictional drag on the near-surface wind speed (137). Given a logarithmic wind speed profile within lower troposphere, higher z_{0m} leads to lower near-surface wind speed but higher near-surface wind shear (137, 138), which is consistent with the upstream (local) shear responses in our experiments (thin curves in *SI Appendix*, Fig. S4 *A*, *E*, *I*, and *M*). The upward transport of momentum flux is parameterized within model's planetary boundary layer (PBL) scheme, which is replaced by the Cloud Layers Unified By Binormals (CLUBB) parameterization in CESM2.1.1 (104). Note that our quantitative results may depend on the nature of the boundary layer parameterization in CESM given that the boundary layer is the key mediator of the response to surface forcings. This is not easy to test directly as we are limited to use the parameterization included in CESM. However, our CESM Control run reproduces the climatological convective environments and flow features, suggesting that the model parameterizations including the PBL scheme represent the relevant boundary-layer processes reasonably well. Hence, we expect the qualitative responses to be robust, though the quantitative values of those responses may be sensitive to the choice of different parameterization schemes (or different models).

Idealized GCM Experiments. Starting from the CESM2.1.1 aquaplanet setup (109–111), we develop an idealized configuration including the minimal geographic ingredients expected to be necessary to produce a regional severe thunderstorm hotspot: a midlatitude continent with a western elevated plateau and poleward of a large source of warm moist air (42–44). The smooth experiment (denoted as *aquasmooth*) simulates an aquaplanet with prescribed monthly varying sea surface temperature (SST) and includes an idealized rectangular midlatitude continent with a 3 km north–south oriented narrow plateau along its western edge (Fig. 4*A*). The rough experiment (denoted as *aquarough*) is the same as *aquasmooth* except that the roughness of the tropical ocean surface equatorward of the continent (the hatched area in Fig. 4*B*) is enhanced to the magnitude of forested land. The design of the model bottom boundary is a slab-ocean continent with interactive temperature surrounded by an aquaplanet ocean whose spatial distribution of SST is prescribed to follow a fixed seasonal cycle similar to the present-day Earth.

The prescribed SST is derived from the 1980 to 2014 historical climatological SST of the ERA5 reanalysis data based on the following steps. First, we calculate the ERA5 monthly and zonal mean SST during 1980 to 2014 (denoted as $SST_0(m, \emptyset)$, *SI Appendix*, Fig. S2*I*), where m denotes boreal month from 1 (January) to 12 (December), and $\emptyset$ denotes latitudes from −90 (90°S) to 90 (90°N). Second, as our aquaplanet is symmetric with respect to the equator, we remove the asymmetry of the seasonal cycle in $SST_0(m, \emptyset)$ between the Northern and Southern Hemispheres to produce $SST_1(m, \emptyset)$ (*SI Appendix*, Fig. S2*J*) based on

$$SST_1(m,\emptyset) = \begin{cases} 0.5(SST_0(m,\emptyset) + SST_0(m+6, -\emptyset)), m \le 6 \\ 0.5(SST_0(m,\emptyset) + SST_0(m-6, -\emptyset)), m < 6 \end{cases}. \qquad [7]$$

Third, for simplicity, we follow (109) to fit a simple sin^2 function to $SST_1(m, \emptyset)$, which yields the following equation defining the $SST(m, \emptyset)$ used as the prescribed SST in our idealized experiments (*SI Appendix*, Fig. S2*K*) with $\phi(m) = -0.06 - 9.94\sin(\frac{\pi}{6}m)$ fitting the location in latitude of monthly maximum SST:

$$SST(m, \emptyset) = \begin{cases} -1.65, \ |\emptyset| \ge 85 \\ \max\left\{-1.65, 29 - 31\sin^2\left(\frac{\pi}{2} \bullet \frac{\emptyset - \phi(m)}{85 - 0.5\phi(m)}\right)\right\}, \ |\emptyset| < 85 \text{ and } m \le 6 \\ \max\left\{-1.65, 29 - 31\sin^2\left(\frac{\pi}{2} \bullet \frac{\emptyset - \phi(m)}{85 + 0.5\phi(m)}\right)\right\}, \ |\emptyset| < 85 \text{ and } m < 6 \end{cases}. \qquad [8]$$

The simple continent and the plateau are both covered by a thin slab ocean with reduced saturation specific humidity at the surface, mimicking the constrained wetness of land, and low heat capacity of the continental surface relative to ocean surface, mimicking the lower thermal inertia of land as compared to ocean. The only difference between the continent and plateau is that the surface elevation is 0 m for the continent but 3 km for the plateau (a height in between the average height of the Rockies and the Andes). The present-day Earth's orbital parameters are used to enable both diurnal and seasonal cycles.

Following ref. 139, we set the slab ocean depth of the continent and plateau to be $h_s = 0.05$ m. This is determined by the soil penetration depth (h) in the diurnal timescale ($\omega = 2\pi/86{,}400\ \mathrm{s}^{-1}$): $h = \sqrt{2D/\omega} \approx 0.11$ m for soil thermal diffusivity $D = 0.5 \times 10^{-6}\ \mathrm{m}^2\ \mathrm{s}^{-1}$ (139, 140). As the volumetric heat capacity of sea water is constant everywhere in the model to be $4.1 \times 10^6\ \mathrm{J\ m^{-3}\ K^{-1}}$ that is roughly twice the value for soil $1.0 - 3.0 \times 10^6\ \mathrm{J\ m^{-3}\ K^{-1}}$, setting the slab ocean depth h_s to roughly half the value of h ensures that the heat capacity of our simple continent ($2.05 \times 10^5\ \mathrm{J\ m^{-2}\ K^{-1}}$) is roughly equivalent to the heat capacity of soil ($1.1 - 3.3 \times 10^5\ \mathrm{J\ m^{-2}\ K^{-1}}$).

In addition to setting an equivalent heat capacity of soil, we also consider the difference in surface wetness between continent and ocean via reducing the saturation specific humidity (q_{sat}) at the surface of the slab continent and plateau by roughly 50%, similar to refs. 141 and 142. This is modified by setting the parameter $\beta = 0.5$ in the model parameterization of surface latent heat flux. The surface latent heat flux equation is given by $E = \rho_a L_v C_q U\left(\beta q_{sat} - q_a\right)$, where ρ_a is the near-surface air density, $L_v = 2.501 \times 10^6\ \mathrm{J\ kg^{-1}}$ is the latent heat of vaporization of water, $C_q \approx 0.0014$ is the enthalpy exchange coefficient, U is the near-surface wind speed, and q_a is the near-surface air specific humidity. Therefore, β is defined by

$$\beta = \left(\frac{E}{\rho_a L_v C_q U} + q_a\right)\frac{1}{q_{sat}}. \qquad [9]$$

We may estimate the value of β based on Eq. **9** using the ERA5 1980 to 2014 climatological annual mean E, ρ_a, 10-m U, 2-m q_a, and q_{sat} for midlatitude ocean, flatlands ($Z_{sfc} < 500$ m) over midlatitude North and South America, and mountains ($Z_{sfc} > 1{,}500$ m) over midlatitude North and South America, respectively. For the ocean, the model takes $\beta = 0.98$ constant. This value is close to $\beta = 0.95$ estimated from substituting the ERA5 midlatitude ocean means of $E = 110\ \mathrm{W\ m^{-2}}$, $\rho_a = 1.2\ \mathrm{kg\ m^{-3}}$, $U = 8.0\ \mathrm{m\ s^{-1}}$, $q_a = 9.5\ \mathrm{g\ kg^{-1}}$, and $q_{sat} = 13.5\ \mathrm{g\ kg^{-1}}$ into Eq. **9**. For the flatlands, we estimate $\beta = 0.77$ by substituting the ERA5 midlatitude North and South American flatland mean values of $E = 65\ \mathrm{W\ m^{-2}}$, $\rho_a = 1.2\ \mathrm{kg\ m^{-3}}$, $U = 8.0\ \mathrm{m\ s^{-1}}$, $q_a = 8.5\ \mathrm{g\ kg^{-1}}$, and $q_{sat} = 13.5\ \mathrm{g\ kg^{-1}}$ into Eq. **9**. For the plateaus, we estimate $\beta = 0.37$ by substituting the ERA5 mid-latitude North and South American mountain mean values of $E = 30\ \mathrm{W\ m^{-2}}$, $\rho_a = 1.0\ \mathrm{kg\ m^{-3}}$, $U = 8.0\ \mathrm{m\ s^{-1}}$, $q_a = 4.0\ \mathrm{g\ kg^{-1}}$, and $q_{sat} = 13.5\ \mathrm{g\ kg^{-1}}$ into Eq. **9**. Note that we use the mean 10 m wind speed over ocean for estimating β over flatland and plateau as well because the surface roughness of slab continents in the model is the same as ocean and thus leads to relatively small difference in their near-surface wind speeds. For simplicity in our experiments, we use $\beta = 0.5$ for both the flat continent and 3 km plateau in our experiments which is broadly consistent with the range of our real-world estimates above.

In *aquarough*, similar to *rough* above, the roughness of the tropical ocean surface upstream of the continent is enhanced to the magnitude of *ctrl* Amazon land by enhancing the drag coefficient (C_d) at the lowest model level (roughly 60 m above the surface) by a factor of 10. We additionally conduct two experiments with the upstream ocean surface roughness enhanced by a factor of 50 and 100 (*SI Appendix*, Fig. S7 *B* and *C*), respectively, to show that our results are not specific to the magnitude of roughness.

Besides modifications detailed above, other model configurations for both experiments are the same as in the default QSC6 configurate within CESM2.1.1 (110, 111). We run both experiments for 14 y on a 1.9° × 2.5° latitude-longitude grid mesh with 32 hybrid sigma-pressure levels, discard the first 4 y for spinup, and analyze the 3-hourly output from the last 10 y.

Ethics and Inclusion Statement.The scope of this research is on continent-scale physics of the atmosphere using computer modeling and thus did not require any direct local interaction, intervention, or impact on local human populations, animal habitats, ecosystems, or cultural artifacts. The project does not carry any location-specific restrictions that would have required prior approval by an ethics board. Relevant published regional research from South American authors on both tornadoes and the Amazon basin is included in our citations as an important part of the foundational motivation for the project.

Data, Materials, and Software Availability. ERA5 reanalysis data (https://rda.ucar.edu/datasets/ds633.0/) (143), US tornado reports (https://www.spc.noaa.gov/wcm/) (144), Southeast South American tornado reports (https://doi.org/10.5281/zenodo.7072781) (132), LIS-OTD lightning data (https://ghrc.nsstc.nasa.gov/pub/lis/climatology/LIS-OTD/HRFC/data/nc/) (145), and CESM2.1.1 model source code (https://www.cesm.ucar.edu/models/cesm2/release_download.html) (146) are publicly available. Data for generating figures in main texts are deposited into PURR (DOI: 10.4231/9E1V-EQ84) (147).

ACKNOWLEDGMENTS. We acknowledge NCAR CISL Cheyenne (DOI: 10.5065/D6RX99HX) and Purdue RCAC for research computing time and infrastructure and developers of Python software packages including numpy, matplotlib, metpy, and xcape. This work was supported by NSF AGS Award Nos. 2146709, 1648681 and 1648629 and NASA FINESST Award No. 19-EARTH20-0216. This material is based upon work supported by the U.S. Department of Energy, Office of Science, Office of Biological & Environmental Research (BER), Regional and Global Model Analysis (RGMA) component of the Earth and Environmental System Modeling Program under Award Numbers DE-SC0022070 and DE-SC0016605, as well as NSF IA 1947282. The National Center for Atmospheric Research (NCAR) is a major facility sponsored by the NSF under Cooperative Agreement No. 1852977. We thank D. T. Dawson II and M. Huber for helpful discussions that improved this work.

1. H. E. Brooks, C. A. Doswell III, Normalized damage from major tornadoes in the United States: 1890–1999. *Weather Forecasting* **16**, 168–176 (2001).
2. W. S. Ashley, Spatial and temporal analysis of tornado fatalities in the United States: 1880–2005. *Weather Forecasting* **22**, 1214–1228 (2007).
3. S. A. Changnon, Tornado losses in the United States. *Nat. Hazards Rev.* **10**, 145–150 (2009).
4. B. Antonescu, D. M. Schultz, A. Holzer, P. Groenemeijer, Tornadoes in Europe: An underestimated threat. *Bull. Am. Meteorol. Soc.* **98**, 713–728 (2017).
5. Z. Meng *et al.*, The deadliest tornado (EF4) in the past 40 years in China. *Weather Forecasting* **33**, 693–713 (2018).
6. J. T. Allen, E. R. Allen, H. Richter, C. Lepore, Australian Tornadoes in 2013: Implications for climatology and forecasting. *Monthly Weather Rev.* **149**, 1211–1232 (2021).
7. M. I. Oliveira, F. S. Puhales, E. L. Nascimento, V. Anabor, Integrated damage, visual, remote sensing, and environmental analysis of a strong tornado in southern Brazil. *Atmos. Res.* **274**, 106188 (2022).
8. P. Markowski, Y. Richardson, *Mesoscale Meteorology in Midlatitudes* (John Wiley & Sons, 2011).
9. E. N. Rasmussen, D. O. Blanchard, A baseline climatology of sounding-derived supercell and tornado forecast parameters. *Weather Forecasting* **13**, 1148–1164 (1998).
10. H. E. Brooks, J. W. Lee, J. P. Craven, The spatial distribution of severe thunderstorm and tornado environments from global reanalysis data. *Atmos. Res.* **67**, 73–94 (2003).
11. V. A. Gensini, W. S. Ashley, Climatology of potentially severe convective environments from the North American Regional Reanalysis. *E-J. Severe Storms Meteorol.* **6**, 1–40 (2011).
12. N. S. Diffenbaugh, M. Scherer, R. J. Trapp, Robust increases in severe thunderstorm environments in response to greenhouse forcing. *Proc. Natl. Acad. Sci. U.S.A.* **110**, 16361–16366 (2013).
13. J. T. Seeley, D. M. Romps, The effect of global warming on severe thunderstorms in the United States. *J. Clim.* **28**, 2443–2458 (2015).
14. M. Taszarek, J. T. Allen, T. Púčik, K. A. Hoogewind, H. E. Brooks, Severe convective storms across Europe and the United States. Part II: ERA5 environments associated with lightning, large hail, severe wind, and tornadoes. *J. Clim.* **33**, 10263–10286 (2020).
15. F. Li, D. R. Chavas, K. A. Reed, D. T. Dawson II, Climatology of severe local storm environments and synoptic-scale features over North America in ERA5 reanalysis and CAM6 simulation. *J. Clim.* **33**, 8339–8365 (2020).
16. M. Taszarek, J. T. Allen, H. E. Brooks, N. Pilguj, B. Czernecki, Differing trends in United States and European severe thunderstorm environments in a warming climate. *Bull. Am. Meteorol. Soc.* **102**, E296–E322 (2021).
17. M. Taszarek, J. T. Allen, M. Marchio, H. E. Brooks, Global climatology and trends in convective environments from ERA5 and rawinsonde data. *NPJ Clim. Atmos. Sci.* **4**, 1–11 (2021).
18. C. Lepore, R. Abernathey, N. Henderson, J. T. Allen, M. K. Tippett, Future global convective environments in CMIP6 models. *Earth's Future* **9**, e2021EF002277 (2021).
19. E. N. Rasmussen, Refined supercell and tornado forecast parameters. *Weather Forecasting* **18**, 530–535 (2003).
20. R. L. Thompson, R. Edwards, J. A. Hart, K. L. Elmore, P. Markowski, Close proximity soundings within supercell environments obtained from the Rapid Update Cycle. *Weather Forecasting* **18**, 1243–1261 (2003).
21. J. P. Craven, H. E. Brooks, J. A. Hart, Baseline climatology of sounding derived parameters associated with deep, moist convection. *National Weather Digest* **28**, 13–24 (2004).

22. R. L. Thompson, B. T. Smith, J. S. Grams, A. R. Dean, C. Broyles, Convective modes for significant severe thunderstorms in the contiguous United States. Part II: Supercell and QLCS tornado environments. *Weather Forecasting* **27**, 1136–1154 (2012).
23. N. S. Diffenbaugh, M. Scherer, R. J. Trapp, Robust increases in severe thunderstorm environments in response to greenhouse forcing. *Proc. Natl. Acad. Sci. U.S.A.* **110**, 16361–16366 (2013).
24. B. E. Coffer, M. D. Parker, R. L. Thompson, B. T. Smith, R. E. Jewell, Using near-ground storm relative helicity in supercell tornado forecasting. *Weather Forecasting* **34**, 1417–1435 (2019).
25. B. E. Coffer, M. Taszarek, M. D. Parker, Near-ground wind profiles of tornadic and nontornadic environments in the United States and Europe from ERA5 reanalyses. *Weather Forecasting* **35**, 2621–2638 (2020).
26. B. E. Coffer, M. D. Parker, J. M. Peters, A. R. Wade, Supercell low-level mesocyclones: Origins of inflow and vorticity. *Monthly Weather Rev.* **151**, 2205–2232 (2023).
27. M. K. Tippett, J. T. Allen, V. A. Gensini, H. E. Brooks, Climate and hazardous convective weather. *Curr. Clim. Change Rep.* **1**, 60–73 (2015).
28. M. K. Tippett, C. Lepore, J. E. Cohen, More tornadoes in the most extreme US tornado outbreaks. *Science* **354**, 1419–1423 (2016).
29. J. B. Elsner, T. Fricker, Z. Schroder, Increasingly powerful tornadoes in the United States. *Geophys. Res. Lett.* **46**, 392–398 (2019).
30. T. T. Fujita, Tornadoes around the world. *Weatherwise* **26**, 56–83 (1973).
31. A. M. Goliger, R. V. Milford, A review of worldwide occurrence of tornadoes. *J. Wind Eng. Ind. Aerodyn.* **74**, 111–121 (1998).
32. H. E. Brooks, C. A. Doswell III, Some aspects of the international climatology of tornadoes by damage classification. *Atmos. Res.* **56**, 191–201 (2001).
33. M. A. Silva Dias, An increase in the number of tornado reports in Brazil. *Weather, Clim. Soc.* **3**, 209–217 (2011).
34. K. L. Rasmussen, M. D. Zuluaga, R. A. Houze Jr., Severe convection and lightning in subtropical South America. *Geophys. Res. Lett.* **41**, 7359–7366 (2014).
35. J. T. Allen, E. R. Allen, A review of severe thunderstorms in Australia. *Atmos. Res.* **178**, 347–366 (2016).
36. J. Chen *et al.*, Tornado climatology of China. *Int. J. Climatol.* **38**, 2478–2489 (2018).
37. D. M. Sills *et al.*, The northern tornadoes project: Uncovering Canada's true tornado climatology. *Bull. Am. Meteorol. Soc.* **101**, E2113–E2132 (2020).
38. M. Taszarek *et al.*, Severe convective storms across Europe and the United States. Part I: Climatology of lightning, large hail, severe wind, and tornadoes. *J. Clim.* **33**, 10239–10261 (2020).
39. R. Zhou, Z. Meng, L. Bai, Differences in tornado activities and key tornadic environments between China and the United States. *Int. J. Climatol.* **42**, 367–384 (2022).
40. C. Zhang, M. Xue, K. Zhu, X. Yu, Climatology of Significant Tornadoes within China and Comparison of Tornado Environments between United States and China. *Monthly Weather Rev.* **151**, 465–484 (2022).
41. M. Maas *et al.*, The Tornado Archive: Compiling and Visualizing a Worldwide, Digitized Tornado Database. *Bull. Amer. Meteor. Soc.*, in press (2024), 10.1175/BAMS-D-23-0123.1.
42. T. N. Carlson, S. G. Benjamin, G. S. Forbes, Y. F. Li, Elevated mixed layers in the regional severe storm environment: Conceptual model and case studies. *Monthly Weather Rev.* **111**, 1453–1474 (1983).
43. K. A. Emanuel, *Atmospheric Convection* (Oxford University Press on Demand, 1994).
44. F. Li, D. R. Chavas, K. A. Reed, N. Rosenbloom, D. T. Dawson II, The role of elevated terrain and the Gulf of Mexico in the production of severe local storm environments over North America. *J. Clim.* **34**, 7799–7819 (2021).
45. H. Wexler, A boundary layer interpretation of the low-level jet. *Tellus* **13**, 368–378 (1961).
46. M. Ting, H. Wang, The role of the North American topography on the maintenance of the Great Plains summer low-level jet. *J. Atmos. Sci.* **63**, 1056–1068 (2006).
47. T. R. Parish, L. D. Oolman, On the role of sloping terrain in the forcing of the Great Plains low-level jet. *J. Atmos. Sci.* **67**, 2690–2699 (2010).
48. W. D. Bonner, Climatology of the low level jet. *Monthly Weather Rev.* **96**, 833–850 (1968).
49. C. D. Whiteman, X. Bian, S. Zhong, Low-level jet climatology from enhanced rawinsonde observations at a site in the southern Great Plains. *J. Appl. Meteorol.* **36**, 1363–1376 (1997).
50. A. K. Blackadar, Boundary layer wind maxima and their significance for the growth of nocturnal inversions. *Bull. Am. Meteorol. Soc.* **38**, 283–290 (1957).
51. J. R. Holton, The diurnal boundary layer wind oscillation above sloping terrain. *Tellus* **19**, 200–205 (1967).
52. X. Jiang, N. C. Lau, I. M. Held, J. J. Ploshay, Mechanisms of the Great Plains low-level jet as simulated in an AGCM. *J. Atmos. Sci.* **64**, 532–547 (2007).
53. Y. Du, R. Rotunno, A simple analytical model of the nocturnal low-level jet over the Great Plains of the United States. *J. Atmos. Sci.* **71**, 3674–3683 (2014).
54. A. Shapiro, E. Fedorovich, S. Rahimi, A unified theory for the Great Plains nocturnal low-level jet. *J. Atmos. Sci.* **73**, 3037–3057 (2016).
55. R. W. Arritt *et al.*, The great plains low-level jet during the warm season of 1993. *Monthly Weather Rev.* **125**, 2176–2192 (1997).
56. H. M. Helfand, S. D. Schubert, Climatology of the simulated Great Plains low-level jet and its contribution to the continental moisture budget of the United States. *J. Clim.* **8**, 784–806 (1995).
57. M. J. Molina, J. T. Allen, On the moisture origins of tornadic thunderstorms. *J. Clim.* **32**, 4321–4346 (2019).
58. R. W. Higgins, K. C. Mo, S. D. Schubert, The moisture budget of the central United States in spring as evaluated in the NCEP/NCAR and the NASA/DAO reanalyses. *Monthly Weather Rev.* **124**, 939–963 (1996).
59. J. E. Chu, A. Timmermann, J. Y. Lee, North American April tornado occurrences linked to global sea surface temperature anomalies. *Sci. Adv.* **5**, eaaw9950 (2019).
60. J. M. Lanicci, T. T. Warner, A synoptic climatology of the elevated mixed-layer inversion over the southern Great Plains in spring. Part I: Structure, dynamics, and seasonal evolution. *Weather Forecasting* **6**, 181–197 (1991).
61. J. M. Lanicci, T. T. Warner, A synoptic climatology of the elevated mixed-layer inversion over the southern Great Plains in spring. Part III: Relationship to severe-storms climatology. *Weather Forecasting* **6**, 214–226 (1991).
62. B. Z. Ribeiro, L. F. Bosart, Elevated mixed layers and associated severe thunderstorm environments in South and North America. *Monthly Weather Rev.* **146**, 3–28 (2018).
63. E. Williams *et al.*, Contrasting convective regimes over the Amazon: Implications for cloud electrification. *J. Geophys. Res.: Atmos.* **107**, LBA-50 (2002).
64. R. J. Van der Ent, H. H. Savenije, B. Schaefli, S. C. Steele-Dunne, Origin and fate of atmospheric moisture over continents. *Water Resour. Res.* **46**, W09525 (2010).
65. N. Insel, C. J. Poulsen, T. A. Ehlers, Influence of the Andes Mountains on South American moisture transport, convection, and precipitation. *Clim. Dyn.* **35**, 1477–1492 (2010).
66. C. J. Poulsen, T. A. Ehlers, N. Insel, Onset of convective rainfall during gradual late Miocene rise of the central Andes. *Science* **328**, 490–493 (2010).
67. C. M. Campetella, C. S. Vera, The influence of the Andes mountains on the South American low-level flow. *Geophys. Res. Let.* **29**, 7-7-1-4 (2002).
68. C. R. Sasaki, A. K. Rowe, L. A. McMurdie, K. L. Rasmussen, New Insights into the South American low-level jet from RELAMPAGO observations. *Monthly Weather Rev.* **150**, 1247–1271 (2022).
69. P. Salio, N. M. Nicolini, A. C. Saulo, Chaco low-level jet events characterization during the austral summer season. *J. Geophys. Res.: Atmos.* **107**, ACL-32 (2002).
70. M. E. Seluchi, A. C. Saulo, M. Nicolini, P. Satyamurty, The northwestern Argentinean low: A study of two typical events. *Monthly Weather Rev.* **131**, 2361–2378 (2003).
71. C. Vera *et al.*, The South American low-level jet experiment. *Bull. Am. Meteorol. Soc.* **87**, 63–78 (2006).
72. J. A. Martinez, F. Dominguez, Sources of atmospheric moisture for the La Plata River basin. *J. Clim.* **27**, 6737–6753 (2014).
73. A. M. Varuolo-Clarke, A. P. Williams, J. E. Smerdon, M. Ting, D. A. Bishop, Influence of the South American low-level jet on the austral summer precipitation trend in southeastern South America. *Geophys. Res. Lett.* **49**, e2021GL096409 (2022).
74. J. A. Marengo, W. R. Soares, C. Saulo, M. Nicolini, Climatology of the low-level jet east of the Andes as derived from the NCEP–NCAR reanalyses: Characteristics and temporal variability. *J. Clim.* **17**, 2261–2280 (2004).
75. K. L. Rasmussen, R. A. Houze Jr., Convective initiation near the Andes in subtropical South America. *Monthly Weather Rev.* **144**, 2351–2374 (2016).
76. R. S. Schumacher *et al.*, Convective-storm environments in subtropical South America from high-frequency soundings during RELAMPAGO-CACTI. *Monthly Weather Rev.* **149**, 1439–1458 (2021).
77. R. J. Trapp *et al.*, Multiple-platform and multiple-Doppler radar observations of a supercell thunderstorm in South America during RELAMPAGO. *Monthly Weather Rev.* **148**, 3225–3241 (2020).
78. P. Salio, M. Nicolini, E. J. Zipser, Mesoscale convective systems over southeastern South America and their relationship with the South American low-level jet. *Monthly Weather Rev.* **135**, 1290–1309 (2007).
79. J. P. Mulholland, S. W. Nesbitt, R. J. Trapp, K. L. Rasmussen, P. V. Salio, Convective storm life cycle and environments near the Sierras de Córdoba, Argentina. *Monthly Weather Rev.* **146**, 2541–2557 (2018).
80. Z. S. Bruick, K. L. Rasmussen, D. J. Cecil, Subtropical South American hailstorm characteristics and environments. *Monthly Weather Rev.* **147**, 4289–4304 (2019).
81. E. J. Zipser, D. J. Cecil, C. Liu, S. W. Nesbitt, D. P. Yorty, Where are the most intense thunderstorms on Earth? *Bull. Am. Meteorol. Soc.* **87**, 1057–1072 (2006).
82. R. A. Houze Jr., K. L. Rasmussen, M. D. Zuluaga, S. R. Brodzik, The variable nature of convection in the tropics and subtropics: A legacy of 16 years of the Tropical Rainfall Measuring Mission satellite. *Rev. Geophys.* **53**, 994–1021 (2015).
83. M. Peterson, Where are the most extraordinary lightning megaflashes in the Americas? *Bull. Am. Meteorol. Soc.* **102**, E660–E671 (2021).
84. D. Veloso-Aguila, K. L. Rasmussen, E. D. Maloney, Tornadoes in Southeast South America: Mesoscale to Planetary-Scale Environments. *Monthly Weather Rev.* **152**, 295–318 (2023).
85. L. O. dos Santos, E. L. Nascimento, J. T. Allen, Discriminant analysis for severe storm environments in South-central Brazil. *Monthly Weather Rev.* **151**, 2659–2681 (2023).
86. P. Salio *et al.*, Towards a South American High Impact Weather Reports Database. *Bull. Amer. Meteor. Soc.*, in press (2024), 10.1175/BAMS-D-23-0063.1.
87. S. W. Nesbitt *et al.*, A storm safari in subtropical South America: Proyecto RELAMPAGO. *Bull. Am. Meteorol. Soc.* **102**, E1621–E1644 (2021).
88. J. O. Piersante, K. L. Rasmussen, R. S. Schumacher, A. K. Rowe, L. A. McMurdie, A synoptic evolution comparison of the smallest and largest MCSs in subtropical South America between spring and summer. *Monthly Weather Rev.* **149**, 1943–1966 (2021).
89. F. M. Piscitelli, J. J. Ruiz, P. Negri, P. Salio, A multiyear radar-based climatology of supercell thunderstorms in Central-Eastern Argentina. *Atmos. Res.* **277**, 106283 (2022).
90. C. M. Mead, R. L. Thompson, Environmental characteristics associated with nocturnal significant-tornado events in the Great Plains. *E-J. Severe Storms Meteorol.* **6**, 1–35 (2011).
91. E. de Lima Nascimento, G. Held, A. M. Gomes, A multiple-vortex tornado in southeastern Brazil. *Monthly Weather Rev.* **142**, 3017–3037 (2014).
92. V. Ferreira, V. Goede, E. de Lima Nascimento, An environmental and polarimetric study of the 19 November 2015 supercell and multiple-vortex tornado in Marechal Cândido Rondon, southern Brazil. *Meteorol. Atmos. Phys.* **134**, 1–25 (2022).
93. A. K. Kis, J. M. Straka, Nocturnal tornado climatology. *Weather Forecasting* **25**, 545–561 (2010).
94. S. J. Weaver, S. Baxter, A. Kumar, Climatic role of North American low-level jets on US regional tornado activity. *J. Clim.* **25**, 6666–6683 (2012).
95. M. N. Rocque, K. L. Rasmussen, The impact of topography on the environment and life cycle of weakly and strongly forced MCSs during RELAMPAGO. *Monthly Weather Rev.* **150**, 2317–2338 (2022).
96. H. Wang, R. Fu, Influence of cross-Andes flow on the South American low-level jet. *J. Clim.* **17**, 1247–1262 (2004).
97. F. Li, On the production of severe convective storm environments in North and South America (Purdue University, 2023).
98. S. Saatchi, E. Rodriguez, S. Denning, R. Dubayah, "LBA-ECO LC-15 Aerodynamic Roughness Maps of Vegetation Canopies, Amazon Basin, Oak Ridge National Laboratory Distributed Active Archive Center" (Oak Ridge, Tennessee, USA, 2013, 2000), 10.3334/ORNLDAAC/1182.
99. R. A. S. D. Santana, C. Q. Dias-Júnior, R. S. D. Vale, J. Tóta, D. R. Fitzjarrald, Observing and modeling the vertical wind profile at multiple sites in and above the Amazon rain forest canopy. *Adv. Meteorol.* **2017**, 5436157 (2017).
100. Z. Hua, D. R. Chavas, The empirical dependence of tornadogenesis on elevation roughness: Historical record analysis using Bayes's law in Arkansas. *J. Appl. Meteorol. Clim.* **58**, 401–411 (2019).
101. J. Eiras-Barca *et al.*, Changes in South American hydroclimate under projected Amazonian deforestation. *Ann. N.Y. Acad. Sci.* **1472**, 104–122 (2020).
102. R. Meier *et al.*, Impacts of a revised surface roughness parameterization in the Community Land Model 5.1. *Geosci. Model Dev.* **15**, 2365–2393 (2022).
103. H. Hersbach *et al.*, The ERA5 global reanalysis. *Q. J. R. Meteorol. Soc.* **146**, 1999–2049 (2020).

104. G. Danabasoglu *et al.*, The community earth system model version 2 (CESM2). *J. Adv. Model. Earth Syst.* **12**, e2019MS001916 (2020).
105. K. D. Sherburn, M. D. Parker, J. R. King, G. M. Lackmann, Composite environments of severe and nonsevere high-shear, low-CAPE convective events. *Weather Forecasting* **31**, 1899–1927 (2016).
106. V. A. Gensini, H. E. Brooks, Spatial trends in United States tornado frequency. *NPJ Clim. Atmos. Sci.* **1**, 1–5 (2018).
107. Z. Pan, M. Segal, R. W. Arritt, Role of topography in forcing low-level jets in the central United States during the 1993 flood-altered terrain simulations. *Monthly Weather Rev.* **132**, 396–403 (2004).
108. H. Bechis, P. Salio, J. J. Ruiz, Drylines in Argentina: Synoptic climatology and processes leading to their genesis. *Monthly Weather Rev.* **148**, 111–129 (2020).
109. R. B. Neale, B. J. Hoskins, A standard test for AGCMs including their physical parametrizations: I: The proposal. *Atmos. Sci. Lett.* **1**, 101–107 (2000).
110. B. Medeiros, D. L. Williamson, J. G. Olson, Reference aquaplanet climate in the Community Atmosphere Model, Version 5. *J. Adv. Model. Earth Syst.* **8**, 406–424 (2016).
111. B. Medeiros, Aquaplanets as a framework for examination of aerosol effects. *J. Adv. Model. Earth Syst.* **12**, e2019MS001874 (2020).
112. M. W. Smith, Roughness in the earth sciences. *Earth-Science Rev.* **136**, 202–225 (2014).
113. P. Tuckman, V. Agard, K. Emanuel, Evolution of convective energy and inhibition before instances of large CAPE. *Monthly Weather Rev.* **151**, 321–338 (2023).
114. Q. Jiang, D. T. Dawson, The impact of surface drag on the structure and evolution of surface boundaries associated with tornadogenesis in simulated supercells. *Monthly Weather Rev.* **151**, 3037–3061 (2023).
115. C. Hoorn *et al.*, Amazonia through time: Andean uplift, climate change, landscape evolution, and biodiversity. *Science* **330**, 927–931 (2010).
116. X. Li, H. Tian, S. Pan, C. Lu, Four-century history of land transformation by humans in the United States: 1630–2020. *Earth Syst. Sci. Data Discussions* **15**, 1005–1035 (2022).
117. T. A. Shaw, O. Miyawaki, A. Donohoe, Stormier Southern Hemisphere induced by topography and ocean circulation. *Proc. Natl. Acad. Sci. U.S.A.* **119**, e2123512119 (2022).
118. J. M. Peters *et al.*, Disentangling the influences of storm-relative flow and horizontal streamwise vorticity on low-level mesocyclones in supercells. *J. Atmos. Sci.* **80**, 129–149 (2023).
119. R. J. Trapp, G. R. Marion, S. W. Nesbitt, The regulation of tornado intensity by updraft width. *J. Atmos. Sci.* **74**, 4199–4211 (2017).
120. P. M. Markowski, Y. P. Richardson, The influence of environmental low-level shear and cold pools on tornadogenesis: Insights from idealized simulations. *J. Atmos. Sci.* **71**, 243–275 (2014).
121. W. S. Ashley, A. M. Haberlie, V. A. Gensini, The Future of Supercells in the United States. *Bull. Am. Meteorol. Soc.* **104**, E1–E21 (2023).
122. M. Woods, R. Trapp, H. M. Mallinson, The impact of human-induced climate change on future tornado intensity as revealed through multi-scale modeling. *Geophys. Res. Lett.* **50**, e2023GL104796 (2023).
123. M. E. O'Neill, L. Orf, G. M. Heymsfield, K. Halbert, Hydraulic jump dynamics above supercell thunderstorms. *Science* **373**, 1248–1251 (2021).
124. A. F. Prein, Thunderstorm straight line winds intensify with climate change. *Nat. Clim. Change* **13**, 1353–1359 (2023).
125. F. Dominguez *et al.*, Advancing South American water and climate science through multi-decadal convection-permitting modeling. *Bull Am. Meteorol. Soc.* **105**, E32–E44 (2023).
126. J. M. Peters, D. R. Chavas, C. Y. Su, H. Morrison, B. E. Coffer, An analytic formula for entraining CAPE in mid-latitude storm environments. *J. Atmos. Sci.* **80**, 2165–2186 (2023).
127. N. A. Goldacker, M. D. Parker, Assessing the comparative effects of storm-relative helicity components within right-moving supercell environments. *J. Atmos. Sci.* **80**, 2805–2822 (2023).
128. A. K. Anderson-Frey, Y. P. Richardson, A. R. Dean, R. L. Thompson, B. T. Smith, Characteristics of tornado events and warnings in the southeastern United States. *Weather Forecasting* **34**, 1017–1034 (2019).
129. M. J. Bunkers, B. A. Klimowski, J. W. Zeitler, R. L. Thompson, M. L. Weisman, Predicting supercell motion using a new hodograph technique. *Weather Forecasting* **15**, 61–79 (2000).
130. R. M. May *et al.*, MetPy: A meteorological Python library for data analysis and visualization. *Bull. Am. Meteorol. Soc.* **103**, E2273–E2284 (2022).
131. M. K. Tippett, C. Lepore, W. J. Koshak, T. Chronis, B. Vant-Hull, Performance of a simple reanalysis proxy for US cloud-to-ground lightning. *Int. J. Climatol.* **39**, 3932–3946 (2009).
132. D. Veloso-Aguila, Tornado Reports in Southeast South America (Version 1). Zenodo. http://doi.org/10.5281/zenodo.7072781. Accessed 15 October 2022.
133. C. K. Potvin, C. Broyles, P. S. Skinner, H. E. Brooks, Improving estimates of US tornado frequency by accounting for unreported and underrated tornadoes. *J. Appl. Meteorol. Climatol.* **61**, 909–930 (2022).
134. J. W. Hurrell, J. J. Hack, D. Shea, J. M. Caron, J. Rosinski, A new sea surface temperature and sea ice boundary dataset for the Community Atmosphere Model. *J. Clim.* **21**, 5145–5153 (2008).
135. D. R. Chavas, F. Li, Biases in CMIP6 historical US severe convective storm environments driven by biases in mean-state near-surface moist static energy. *Geophys. Res. Lett.* **49**, e2022GL098527 (2022).
136. M. L. Oliveira, E. L. Nascimento, C. Kannenberg, A new look at the identification of low-level jets in South America. *Monthly Weather Rev.* **146**, 2315–2334 (2018).
137. R. B. Stull, *An Introduction to Boundary Layer Meteorology* (Springer Science & Business Media, 1988), **vol. 13**.
138. T. A. Coleman, K. R. Knupp, P. T. Pangle, The effects of heterogeneous surface roughness on boundary layer kinematics and wind shear. *E-J. Severe Storms Meteorol.* **16**, 1–29 (2021).
139. T. W. Cronin, K. A. Emanuel, P. Molnar, Island precipitation enhancement and the diurnal cycle in radiative-convective equilibrium. *Q. J. R. Meteorol. Soc.* **141**, 1017–1034 (2015).
140. T. E. Ochsner, R. Horton, T. Ren, A new perspective on soil thermal properties. *Soil Sci. Soc. Am. J.* **65**, 1641–1647 (2001).
141. T. W. Cronin, D. R. Chavas, Dry and semidry tropical cyclones. *J. Atmos. Sci.* **76**, 2193–2212 (2019).
142. B. Fan, Z. Tan, T. A. Shaw, E. S. Kite, Reducing surface wetness leads to tropical hydrological cycle regime transition. *Geophys. Res. Lett.* **48**, e2020GL090746 (2021).
143. European Centre for Medium-Range Weather Forecasts, "ERA5 Reanalysis (0.25 Degree Latitude-Longitude Grid)." Computational and Information Systems Laboratory at the National Center for Atmospheric Research. https://doi.org/10.5065/BH6N-5N20. Accessed 15 April 2020.
144. National Weather Service, "Severe Weather Database Files (1950-2018)." Storm Prediction Center. https://www.spc.noaa.gov/wcm/. Accessed 15 October 2019.
145. D. J. Cecil, "LIS/OTD Gridded Lightning Climatology Data Collection." NASA EOSDIS Global Hydrology Resource Center. https://ghrc.nsstc.nasa.gov/pub/lis/climatology/. Accessed 12 July 2022.
146. CESM Software Engineering Group, "The Community Earth System Model (CESM) version 2.1.1." National Science Foundation National Center for Atmospheric Research. https://www.cesm.ucar.edu/models/cesm2/release_download.html. Accessed 21 January 2020.
147. F. Li, D. R. Chavas, B. Medeiros, K. A. Reed, K. L. Rasmussen, "Dataset for Li et al. 2024, PNAS Upstream surface roughness and terrain are strong drivers of contrast in tornado potential between North and South America." Purdue University Research Repository. http://doi.org/10.4231/9E1V-EQ84. Deposited 23 May 2024.